

Contents

CERTIFICATE	Error! Bookmark not defined.
DECLARATION BY THE CANDIDATE	Error! Bookmark not defined.
Acknowledgments	vii
Contents	xi
LIST OF FIGURES	xvii
LIST OF TABLES	xxvii
LIST OF SYMBOLS AND ABBREVIATIONS	xxix
PREFACE	xxxiii
CHAPTER 1: Introduction and Literature Review	1
1.1 Energy Scenario	1
1.2 Fuel Cells: An Overview	3
1.2.1 Design and working of Fuel Cell.....	4
1.2.2 Type of Fuel Cell.....	5
1.3 Solid Oxide Fuel Cell (SOFC)	6
1.3.1 The basic operation of SOFC	8
1.3.2 Components of SOFC.....	8
1.4 Reaction and Kinetic mechanism for the cathode in SOFC	12
1.4.1 Mechanism of Oxygen Reduction Reaction (ORR)	13
1.4.2 Mechanism for Oxygen Evolution Reaction (OER).....	16
1.5 Materials Selection for Cathode of SOFC	18
1.5.1 Magnetite based cathodes.....	18
1.5.2 Ferrite based cathodes	20
1.5.3 Nickelate based cathodes.....	20
1.5.4 Cobaltite based cathode.....	21
1.5.5 Ferro-cobaltite based cathode.....	22
1.6 State of the Art: Cobaltite based cathode	23
1.6.1 Perovskite structure	23
1.6.2 Double Perovskite Structure.....	25
1.7 Layered perovskite ($\text{LnBaCo}_2\text{O}_{6-\delta}$).....	26
1.7.1 Overview of $\text{PrBaCo}_2\text{O}_{6-\delta}$	29

1.8	The objective of the Present Research Work	30
	CHAPTER 2: Materials and Methods	33
2.1	Overview.....	33
2.2	Specification of the Materials used.....	33
2.3	Synthesis of Materials.....	34
2.3.1	Solid-state reaction route (SSR).....	34
2.3.2	Auto-combustion synthesis (ACR).....	36
2.3.3	Pulse Laser Deposition Technique (PLD)	37
2.4	Characterization Techniques.....	39
2.4.1	Thermogravimetric Analysis (TGA).....	39
2.4.2	Differential Scanning Calorimetry (DSC)	40
2.4.3	Bench-Top X-Ray Diffraction (BT-XRD).....	42
2.4.4	Scanning Electron Microscopy (SEM)	44
2.4.5	Transmission Electron Microscopy (TEM)	47
2.4.6	X-ray Photoelectron Spectroscopy (XPS).....	48
2.4.7	Scanning Tunneling Microscopy (STM)	50
2.4.8	Cyclic Voltammetry (CV).....	52
2.4.9	Density Measurement	54
2.5	Methods and Analysis.....	55
2.5.1	Rietveld Refinement Technique.....	55
2.5.2	Software for Analyzing the Obtained Data.....	56
2.6	Theoretical Studies.....	56
2.6.1	Computational Details.....	57
	CHAPTER 3: Porous and highly conducting PrBaCo₂O_{6-δ}: bulk and surface studies of synthesis anomalies.....	61
3.1	Introduction.....	61
3.2	Theoretical background	62
3.2.1	Possible link between microstructure development and Jahn-teller distortion	63
3.2.2	Neumann principle, specific heat and Jahn-Teller distortion.....	63
3.2.3	Estimation/extraction of specific heat, Jahn-Teller distortion and related parameter	65
3.3	Methodology	65
3.3.1	Sample preparation	65
3.3.2	Characterization techniques	66
3.3.3	Computational details	67

3.4	Result and discussion	67
3.4.1	Structural details of the calcined powder	67
3.4.2	Thermal studies of calcined powders	68
3.4.3	Structural studies of sintered pallets.....	69
3.4.4	Microstructural studies of sintered pallets.....	72
3.4.5	TEM micrograph	73
3.4.6	Electrical and electronic studies of sintered sample.....	74
3.4.7	Surface studies of sintered pallets	78
3.4.8	Structural distortion analysis	80
3.4.9	Electronic and phononic contributions.....	83
3.5	Conclusion.....	86
	CHAPTER 4: Compositional effect on Oxygen reduction reaction in Pr excess double perovskite $\text{Pr}_{1+x}\text{Ba}_{1-x}\text{Co}_2\text{O}_{6-\delta}$ cathode materials.....	93
4.1	Introduction	93
4.2	Experimental Procedure	95
4.2.1	Synthesis.....	95
4.2.2	Characterization technique	95
4.3	Results and Discussion.....	96
4.3.1	Tolerance factor.....	96
4.3.2	Structural and microstructural studies	97
4.3.3	X-ray photoelectron spectroscopy studies.....	105
4.3.4	Catalytic studies	108
4.4	Conclusion.....	115
	CHAPTER 5: Catalytic behavior of $\text{Pr}_{1-x}\text{Ba}_{1+x}\text{Co}_2\text{O}_{6-\delta}$ in alkaline medium.....	119
5.1	Introduction	119
5.2	Experimental Procedure	122
5.2.1	Chemicals, Synthesis and measurements	122
5.2.2	Electrode preparation and electrochemical measurements.....	123
5.3	Results and Discussion.....	123
5.3.1	Thermogravimetry analysis	123
5.3.2	Structural and microstructural studies	124
5.3.3	Microstructural studies	126
5.3.4	Electrochemical catalytic activity.....	129
5.3.5	Catalytic activity for OER.....	134

5.4 Conclusion	136
CHAPTER 6: A Comparative study of catalytic behavior of PrBaCo₂O_{6-δ} and Pr_{1.6}Ba_{0.4}Co₂O_{6-δ}:	
Bulk and thin film	141
6.1 Introduction.....	141
6.2 Synthesis and characterization	142
6.3 Results and Discussion	143
6.3.1 Structural Studies	143
6.3.2 Optical microscopy observation and Surface morphology	144
6.3.3 Catalytic Studies	145
6.4 Conclusion	149
CHAPTER 7: Conclusions and Future Scopes	153
7.1 Conclusion of the Present Investigation.....	153
7.2 Scope for Future Work.....	156
References.....	157
List of Publications	175

LIST OF FIGURES

		Page No.
Chapter I	Introduction and Literature review	
Fig. 1.1	(a) Total energy consumption in India from 1990 to 2020. (b) Breakdown of energy by various sources globally	2
Fig. 1.2	Schematic diagram of a fuel cell (a) Oxide ion conducting electrolyte and (b) Proton conducting electrolyte	4
Fig. 1.3	Schematic representation of Triple Phase Boundary	13
Fig. 1.4	Schematic illustration of three reaction paths for the cathodic reaction	15
Fig. 1.5	Number of publications in the last 5 years for the keyword of cathode materials	22
Fig. 1.6	(a) Atomic structure in mixed conducting perovskite, left image represents ions' position in a cubic structure, and right image represents the BO ₆ octahedra with oxygen vacancy migration path	23
Fig. 1.7	Crystal structure of layered perovskite LnBaCo ₂ O _{6-δ}	24
Fig. 1.8	Crystal structure of LnBaCo ₂ O _{6-δ} (Ln=Nd) at various oxygen content	26
Fig. 1.9	Relationship between oxygen-vacancy concentration and A-site cation size differences ($r_{A^{2+}} - r_{A^{3+}}$) (at room-temperature	27
Chapter II	Materials and Methods	
Fig. 2.1	Schematic diagram of solid-state route (SSR) method	35
Fig. 2.2	Schematic diagram of the auto-combustion synthesis method	37
Fig. 2.3	Schematic diagram of pulse laser deposition technique	38
Fig. 2.4	(a) A thermogram curve showing the change of mass of a	40

substance at different temperatures (b) Experimental setup of TGA at Central instrument facility (CIF) IIT (BHU)

Fig. 2.5	Experimental setup of DSC at Central instrument facility (CIF) IIT (BHU)	41
Fig. 2.6	(a) Interpretation of Bragg's law in 2-dimensional crystal lattice (b) Experimental set-up of BTXRD at Central instrumentation facility CIF IIT(BHU)	44
Fig. 2.7	(a) Operating Principle of SEM (b) Experimental setup of SEM at central instrumentation facility CIF IIT(BHU)	46
Fig. 2.8	Experimental set up of the TEM technique at CIF-IIT (BHU), inset shows the sample holder	47
Fig. 2.9	Basic component of monochromatic XPS system	49
Fig. 2.10	(a) Schematic view of STM [Ref. Wikipedia] (b) Experimental set up of STM	51
Fig. 2.11	(a) cyclic voltammogram (b) Experimental set up of Cyclic voltammetry	52
Fig. 2.12	Density measurement kit by Sartorius, BSA2245-CW	54

Chapter III Porous and highly conducting PrBaCo₂O_{6-δ}: bulk and surface studies of synthesis anomalies

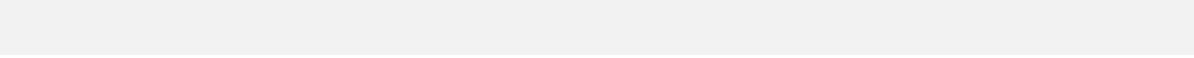
Fig. 3.1	(a) XRD of calcined powder through SSR and ACR techniques (b) indicates the peak corresponding to $2\theta \approx 32^\circ$ (c) Structure of PrBaCo ₂ O _{6-δ} in the b-axis view (d) SEM micrographs of calcined powders (e) mass loss and dm/dT with variation in temperature for the calcined powders (f) change in entropy, ΔS and free energy, ΔG of the calcined powders	69
Fig. 3.2	(a) XRD of sintered palletes is sintered at 1050 °C, 1075 °C, 1100 °C and 1150 °C for 10 h in case of SSR sample and sintered at 1050 °C, 1100 °C, 1150 °C and 1200 °C for 10 h in	70

	case of ACR sample (b) Phase purity of samples prepared by SSR and ACR methods as function of sintering temperature	
Fig. 3.3	(a) Rietveld refinement of the XRD of the optimized SSR and ACR samples (for instance) (a inset) shows the peak corresponding to $2\theta \approx 32^\circ$ showing the pure phase compounds P-SSR at 1050 °C and P-ACR at 1150 °C. (b) One unit cell length along the b-axis possesses three octahedra and can be seen in the a-axis view and (c) SEM images of SSR and ACR samples after sintering	71
Fig. 3.4	(a) TEM micrographs for the SSR sample. (b) Indexed SAED images for the SSR sample. (c) HRTEM images for the SSR sample showing crystal orientation matching well with the structure obtained from Diamond software after Rietveld refinement of the samples. (d) TEM micrographs showing twin domains in the ACR sample. (e) Indexed SAED images for the ACR sample. (f) HRTEM images for the ACR sample showing crystal orientation in the b–c direction in comparison to the a–b direction for the SSR sample.	73
Fig. 3.5.	Wide X-ray Photoelectron spectroscopy (XPS) spectrum for the optimized samples and indexing done using standard look up table.	74
Fig. 3.6	Deconvoluted peaks of Co and O of the SSR and ACR samples showing the presence of satellites and Auger peaks	75
Fig. 3.7	Room temperature conductivity of P-SSR and P-ACR samples	76
Fig. 3.8	Room-temperature voltammograms of P-SSR and P-ACR samples	77
Fig. 3.9	(a) SEM and (b) STM images of the pellet surface after sintering for P-SSR and P-ACR samples, respectively (STM done in constant current mode; the vertical scale bar represents the separation between the surface and the tip of the STM	80

	probe)	
Fig. 3.10	Raman spectra for the P-SSR and P-ACR samples	81
Fig. 3.11	(a and b) Bond angle for the calcined and sintered ACR and SSR samples. The bond angles participating in octahedral tilting around the a-axis and b-axis are θ_α and θ_β shown pictorially in (c and d). The bond angles are designated as O ₇ -Co ₁ -O ₇ as $\theta_{\beta'1}$, O ₇ -Co ₂ -O ₇ as $\theta_{\beta'2}$, Co ₁ -O ₆ -Co ₁ as $\theta_{\alpha161}$ and Co ₂ -O ₅ -Co ₂ as $\theta_{\alpha252}$	82
Fig. 3.12	Cooperative Jahn-Teller distortions in the ACR and SSR samples	83
Fig. 3.13	Variation in C_V versus T: SSR and ACR samples for electronic and phononic behavior estimation, (inset (i)) C_V/T versus T^2 showing better χ^2 for linear fit (inset (ii)) indicating the shift in Schottky anomaly temperature	84
Fig. 3.14	Total and partial DOS for the Co ₂ and O ₇ atoms. The inset shows the matching of PDOS at 0 eV for the SSR sample	85
Fig. 3.15	(a) PDOS states of Co and O showing the interaction from the p-orbital of oxygen to the d-orbital of Co. (b) Band structure of the SSR sample	86
Chapter IV	Compositional effect of oxygen reduction reaction in Pr excess double perovskite Pr_{1+x}Ba_{1-x}Co₂O_{6-δ} cathode materials	
Fig. 4.1	Tolerance factor of the studied compositions (1+x) PrCoO ₃ - (1-x) BaCoO ₃	94
Fig. 4.2	(a, b) Rietveld refined X-ray diffraction patterns of the studied compositions (1+x) PrCoO ₃ - (1-x) BaCoO ₃	96
Fig. 4.3	(a) Phase % of PrBaCo ₂ O _{6-δ} (φ_{Pmmm}) and PrCoO ₃ (φ_{Pnma}) (b) Lattice parameter 'b' corresponding to PrBaCo ₂ O _{6-δ} (φ_{Pmmm}) and PrCoO ₃ (φ_{Pnma}) (b, inset) Orthorhombic distortion	97

	PrBaCo ₂ O _{6-δ} (φ_{Pmmm}) and PrCoO ₃ (φ_{Pnma})	
Fig. 4.4	Specific heat (C_v) of the studied compositions (1+x) PrCoO ₃ - (1-x) BaCoO ₃ showing the presence of two phases PrBaCo ₂ O _{6-δ} and PrCoO ₃	101
Fig. 4.5	SEM micrographs and respective grain size histograms of (1+x) PrCoO ₃ - (1-x) BaCoO ₃	102
Fig. 4.6	Density and Porosity measured through Archmedes' principle of (1+x) PrCoO ₃ - (1-x) BaCoO ₃ (x = 0.2, 0.4, 0.6 and 0.8)	103
Fig. 4.7	Deconvoluted XPS spectra using XPS peak of Pr3d, Co2p and O1s with Shirley background	105
Fig. 4.8	Variation of grain size obtained from Grain size histograms and Pr content observed from EDX and XPS with x	106
Fig. 4.9	Cyclic Voltammetric curves for the (1+x) PrCoO ₃ - (1-x) BaCoO ₃ (respective insets) show the area under the curve is higher for x = 0.6, 4 th quadrant represents the higher V_{oc} and I_{sc} in x = 0.6 sample	107
Fig. 4.10	Cyclic Voltammetric curves for the (1+x) PrCoO ₃ - (1-x) BaCoO ₃ with the different scan rate	108
Fig. 4.11	Variation of i_p vs $v^{1/2}$ as per RS equation for the (1+x) PrCoO ₃ - (1-x) BaCoO ₃	109
Fig. 4.12	Chronoamperometric response for the (1+x) PrCoO ₃ - (1-x) BaCoO ₃ (x = 0.0, 0.6 and x= 0.8)	110
Fig. 4.13	Tafel plot showing E_{corr} , I_{corr} and Corrosion rate (CR) of the (1+x) PrCoO ₃ - (1-x) BaCoO ₃ (x = 0.0, 0.6) compositions (here corrosion rate in mmY stands for mm/year)	111
Chapter V	Catalytic behavior of Pr_{1-x}Ba_{1+x}Co₂O_{6-δ} in alkaline medium	
Fig. 5.1	TGA curve of the Pr _{1-x} Ba _{1+x} Co ₂ O _{6-δ} samples in N ₂ atmosphere	122
Fig. 5.2	X-ray diffractograms of the compositions Pr _{1-x} Ba _{1+x} Co ₂ O _{6-δ} (b) Magnified XRD graph (c) Rietveld refined XRD graph of Pr _{1-x} Ba _{1+x} Co ₂ O _{6-δ} (x=0.0,0.5,0.10 and 0.20)	123

Fig. 5.3	SEM images of $\text{Pr}_{1-x}\text{Ba}_{1+x}\text{Co}_2\text{O}_6$ ($x= 0.0, 0.05, 0.15$ and 0.20)	125
Fig. 5.4	EDX images of $\text{Pr}_{1-x}\text{Ba}_{1+x}\text{Co}_2\text{O}_6$ ($x= 0.0, 0.05, 0.15$ and 0.20)	126
Fig. 5.5	Size distribution of $\text{Pr}_{1-x}\text{Ba}_{1+x}\text{Co}_2\text{O}_6$ by numbers. Dispersant is ethanol	126
Fig. 5.6	Cyclic voltammetry curve for $\text{Pr}_{1-x}\text{Ba}_{1+x}\text{Co}_2\text{O}_{6-\delta}$ at 50 mV/s scan rate	128
Fig. 5.7	Cyclic voltammetry curve for $\text{Pr}_{1-x}\text{Ba}_{1+x}\text{Co}_2\text{O}_{6-\delta}$ with the different scan rate	128
Fig. 5.8	Specific capacity of electrodes at various scan rates	130
Fig. 5.9	The b value corresponding cathodic peak current from CV curves (b)-corresponding RS equation for $x = 0.10$	132
Fig. 5.10	Linear fitting plots of the double layer capacitive current density vs. scan rates	133
Fig. 5.11	Chronopotentiometry behavior of all the electrode samples for 10^4 seconds	134
Chapter VI Comparative study of $\text{PrBaCo}_2\text{O}_{6-\delta}$ and $\text{Pr}_{1.6}\text{Ba}_{0.4}\text{Co}_2\text{O}_{6-\delta}$: bulk and thin film		
Fig. 6.1	X-ray diffraction pattern of $x = 0$ and $x = 0.6$ thin film	141
Fig. 6.2	Optical microscopy images of $x=0$ and $x=0.6$ thin film	142
Fig. 6.3	Topographical AFM images of $x=0$ and $x=0.6$ thin film	142
Fig. 6.4	Cyclic Voltammetric curves for the $x=0$ and $x=0.6$ (bulk and thin film) at scan rate of 50 mV/s	144
Fig. 6.5	Cyclic Voltammetric curves for the $x=0$ and $x=0.6$ (bulk and thin film) at different scan rate	144
Fig. 6.6	Variation of i_p vs $v^{1/2}$ as per RS equation for all the sample	145
Fig. 6.7	Chronoamperometric response for $x = 0$ and $x = 0.6$ (bulk and thin film)	146



LIST OF TABLES

		Page No.
<hr/>		
Chapter I	Introduction and Literature review	
Table 1.1	Comparison of different types of Fuel Cells	7
<hr/>		
Chapter II	Materials and Methods	
Table 2.1	Specifications of the materials used along with their chemical formula, purity, and manufacturer used for the preparation of various samples	34
<hr/>		
Chapter III	Porous and highly conducting cathode material Pr₁BaCo₂O_{6-δ}: bulk and surface studies of synthesis anomalies	
Table 3.1	Lattice parameters and Wyckoff positions for the optimized sintered SSR and ACR samples	72
<hr/>		
Chapter 2V	Compositional effect of oxygen reduction reaction in Pr excess double perovskite Pr_{1+x}Ba_{1-x}Co₂O_{6-δ} cathode materials	
Table 4.1	Rietveld refinement parameter of (1+x) PrCoO ₃ – (1-x)BaCoO ₃	100
Table 4.2	A comparative of commercial and well-known electrodes with the present work.	113

Chapter V	Catalytic behavior of $\text{Pr}_{1-x}\text{Ba}_{1+x}\text{Co}_2\text{O}_{6-\delta}$ in alkaline medium	
Table 5.1	Rietveld refinement parameter for $\text{Pr}_{1+x}\text{Ba}_{1-x}\text{Co}_2\text{O}_{6-\delta}$ ($x=0.05, 0.10$ and 0.20)	124
Table 5.2	Comparision of specific capacitance of well known electrodes with the present work	129

LIST OF SYMBOLS AND ABBREVIATIONS

AFC	Alkaline Fuel Cell
PEMFC	Proton Exchange Membrane Fuel Cell
DMFC	Direct Methanol Fuel Cell
PAFC	Phosphoric Acid Fuel Cell
MCFC	Molten Carbonate Fuel Cell
SOFC	Solid Oxide Fuel Cell
ORR	Oxygen Reduction Reaction
TEC	Thermal Expansion Coefficient
RT	Room temperature
ASR	Area Specific Resistance
MIEC	Mixed Ionic-Electronic Conductor
CV	Cyclic Voltammetry
EIS	Electrochemical Impedance Spectroscopy
IDEP	Isotope Exchange Depth Profile
OER	Oxygen Evolution Reaction
HER	Hydrogen Evolution Reaction
IT-SOFC	Intermediate Temperature Solid Oxide Fuel Cell
YSZ	Yttrium Stabilized Zirconia
CGO	Gadolinium Doped Ceria
PBCO	$\text{PrBaCo}_2\text{O}_{6-\delta}$
DSC	Differential Scanning Calorimetry
TGA	Thermogravimetry analysis
XRD	X-ray diffraction
JCPDS	Joint Committee on Powder Diffraction Standards
SEM	Scanning Electron Microscopy
TEM	Transmission Electron Microscopy

XPS	X-ray Photoelectron Spectroscopy
STM	Scanning Tunneling Microscopy
FWHM	Full width at Half Maximum
SSR	Solid State Route
ACR	Auto Combustion Route
P-SSR	Pallet Synthesized through SSR
P-ACR	Pallet Synthesized through ACR
K	Kelvin
N	Avogadro's Number
JT	Jahn-Teller
ΔG	Gibbs Free Energy
ΔS	Entropy
ΔH	Enthalpy
G	Gram
SAED	Selected Area Electron Diffraction
V	Volt
OD	Orthorhombic Distortion
DFPT	Density Functional Perturbation Theory
DOS	Density of State
HS	High Spin
LS	Low Spin
IS	Intermediate Spin
RS	Randles-Ševčík
CR	Corrosion Rate